Applied Physics Letters

Micrometer-scale InP selectively grown on SOI for fully integrated Si-photonics

Cite as: Appl. Phys. Lett. **117**, 052102 (2020); https://doi.org/10.1063/5.0015130
Submitted: 25 May 2020 . Accepted: 21 July 2020 . Published Online: 04 August 2020

Yu Han, Zhao Yan, Ying Xue, and Kei May Lau

Applied Physics Letters ARTICLE scitation.org/journal/apl

Micrometer-scale InP selectively grown on SOI for fully integrated Si-photonics

Cite as: Appl. Phys. Lett. **117**, 052102 (2020); doi: 10.1063/5.0015130
Submitted: 25 May 2020 · Accepted: 21 July 2020 ·
Published Online: 4 August 2020

View Online Export Citation CrossMark

Yu Han, Zhao Yan, Ying Xue, and Kei May Lau[a)]

AFFILIATIONS

Department of Electronic and Computer Engineering, Hong Kong University of Science and Technology, Clear Water Bay, Kowloon, Hong Kong, China

[a)]Author to whom correspondence should be addressed: eekmlau@ust.hk. **Tel.:** (852)23587049. **Fax:** (852) 23581485

ABSTRACT

Practical applications of low-defect III–V materials grown on Si require large areas for patterning metal contacts and enhancing design flexibility. Here, we report selective area growth of bufferless and micrometer-scale InP on commercial (001)-oriented silicon-on-insulators. We obtained in-plane, centimeter-long and micrometer-wide InP single crystal stripes right atop the buried oxide layer through leveraging the lateral aspect ratio trapping (lateral ART) growth method. Using the extended InP grown by "lateral ART," we inserted InGaAs quantum wells emitting at the telecom bands. Numerical simulation suggests that the micrometer-scale InP can support the fundamental TE mode with an ultra-low metal-induced propagation loss of 3.2 dB/cm when patterned into ridge waveguides and introducing metal contacts at both ends. Our results here represent a leap toward electrically driven III–V lasers seamlessly interfaced with Si-photonics.

Epitaxial integration of III–V functionalities, such as light emission, modulation, and detection, onto Si-based photonic integrated circuits represents the crux for next-generation fully integrated Si-photonics.[1,2] Over the last decade, tremendous progress has been made in the direct hetero-epitaxy of III–V lasers on industry-standard (001)-oriented Si substrates, with potential integration with Si complementary-metal-oxide-semiconductor (CMOS) technologies. Research attention has been focused on reducing the defect density of the epitaxial III–V materials, thereby improving the device performance and reliability.[3,4] As the figures-of-merit of the lasers grown on Si continue to improve and approach the industrial requirement,[5] the next question is how to seamlessly couple the III–V-based active elements with Si-based passive components. In the blanket epitaxy of III–V quantum dot lasers on Si with the best demonstrated device performances, several micrometer-thick III–V buffer layers are employed to minimize the defect densities.[6–8] Efficient light interfacing between the III–V lasers on top of the thick buffer and the Si waveguides underneath remains a challenge and is yet to be resolved. As an alternative, selective growth of III–V materials on pre-patterned Si/SOI substrates avoids the thick buffers and confines the crystalline defects induced by lattice mismatch at the III–V/Si hetero-interface.[9–12] This "bufferless" feature facilitates efficient light coupling from the III–V lasers into the Si-waveguides. Nevertheless, the dimension of III–V alloys selectively grown on Si is usually restricted at the sub-micrometer scale, and the fabricated III–V lasers often require optical excitation.[13–19] The main challenge in realizing electrically driven lasers lies in how to extend the material volume of the selectively grown III–V materials, leading to minimal propagation loss induced by the metal contacts.[20]

Here, we address this challenge through the direct growth of micrometer-scale InP alloys on (001)-oriented SOI wafers leveraging our previously reported lateral ART method.[21] The large dimension of the selectively grown InP is enabled by the creation of ultra-wide trenches sandwiched by oxides on the SOI [Fig. 1(a)] and the pitch expansion of the patterned SOI to warrant the diffusion of growth precursors into the deep oxide trenches [Fig. 1(b)]. The resultant InP on SOI manifests an in-plane configuration and features a width up to 3.0 μm, a thickness of 500 nm, and a length up to 1.5 cm. Extensive transmission electron microscopy (TEM) investigation reveals the confinement of crystalline defects at the III–V/Si interface and the dislocation-free characteristic of the InP alloy away from the hetero-interface. We also observed strong photoluminescence emission at the telecom bands by embedding InGaAs quantum wells inside the InP. We detected an ultra-low metal-induced propagation loss of 3.2 dB/cm when patterning the InP into ridge waveguides and introducing metal contacts at both ends. These results mark an important step toward realizing integrated electrically driven III–V lasers onto Si-photonics platforms.

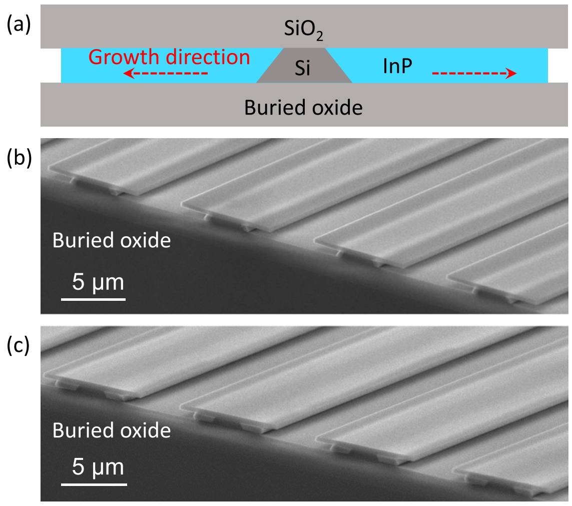

FIG. 1. (a) Schematic showing the growth of micrometer-scale InP inside ultra-deep oxide trenches using the lateral ART growth technique. The red dotted arrow denotes the growth direction. (b) Tilted-view SEM photo of 500 nm wide InP grown on SOI. (c) Tilted-view SEM photo of 2.0 μm wide InP grown on SOI.

Figure 1(a) schematically depicts the growth scheme of the lateral ART technique. We created the lateral oxide trenches using selective wet etching (10% KOH at 80 °C). Depending on the Si etching condition and the pattern size, the undercut of the patterned Si (lateral depth of the trenches) varies from a few hundred nanometers to a few micrometers. InP on Si hetero-epitaxy initiates from the exposed (111)-Si surfaces and evolves laterally along the trench direction. As a result, the epitaxial InP features an in-plane configuration with the Si device layer of the SOI, and the width ranges from the nanometer-scale up to the micrometer-scale. Growing III–V on {111}-oriented Si facets precludes the formation of anti-phase boundaries,[22] and the large aspect ratio of the oxide trench effectively blocks the propagation of crystalline defects into the device region away from the interface. The large lattice mismatch between InP and Si can be accommodated through the formation of highly twinned regions at the III–V/Si interface instead of more detrimental threading dislocations that propagate. We performed the material growth using a metal organic chemical vapor deposition (MOCVD) system with a horizontal reactor (AIXTRON 200/4). We started by thermally annealing the sample at 800 °C in a H_2 ambient for 15 min to desorb the residual oxide at the {111} Si surfaces. Afterward, a thin layer of GaAs nucleation was deposited at 400 °C, followed by InP nucleation at 430 °C. The reactor temperature was then ramped to 630 °C for the InP main layer growth. The growth precursors used were triethylgallium (TEGa), tertiarybutylarsine (TBA), trimethylindium (TMIn), and tertiarybutylphosphine (TBP), and the deposition pressure was 50 mbar. The average growth rate of the InP is around 17 nm/min, and the value increases as the InP grows toward the opening of the lateral trench. Figure 1(b) presents a tilted-view scanning electron microscopy (SEM) image of 500 nm wide InP selectively grown inside the lateral trenches. The growth follows the schematic depicted in Fig. 1(a), and the InP exhibits a uniform morphology along the trench direction. Figure 1(c) displays a SEM photo of 2.0 μm wide InP grown on SOI. As expected, the InP extends laterally along the oxide trench and the width can be readily controlled by adjusting the growth time. Figures 2(a)–2(d) show cross-sectional SEM photos of grown InP with a width of 500 nm, 1.0 μm, 2.0 μm, and 3.0 μm, respectively, highlighting the extension of the epitaxial InP from the nanometer-scale to the micrometer-scale. The lateral dimension of the epitaxial InP could potentially reach tens of micrometers with appropriate growth conditions.[23]

To investigate the crystalline quality of the epitaxial InP and identify the defect necking mechanism of lateral ART with the top and bottom SiO_2 layers to block the propagation of inclined crystalline defects,[4] we prepared InP lamellae with different lateral dimensions using focused ion beam (FIB) milling and examined the specimens using TEM. Figures 3(a) and 3(b) present cross-sectional TEM images of InP on SOI with a width of around 500 nm and 1.0 μm, respectively. Crystalline defects induced by lattice mismatch are confined at the III–V/Si interface, and the InP away from the interface is completely dislocation-free. Figure 3(c) shows a zoomed-in TEM image of the III–V/Si hetero-interface. Lattice mismatch is mainly accommodated through the formation of planar defects along the {111}-oriented Si surface. These planar defects are confined within the initial III–V nucleation and terminated at the top and bottom oxide layers. However, we also detected a few planar defects perpendicular to the Si surface penetrating into the epitaxial InP. This kind of planar defect is accompanied by two partial threading dislocations at both ends and introduces non-radiative recombination centers into the InP crystal. Although these defects will eventually be blocked by the SiO_2 layers, they compromise the defect necking effect of the lateral ART technique and should be minimized via tuning of the nucleation conditions. Figures 3(f) and 3(g) showcase global-view TEM images of InP crystals with a width of 2.0 μm and 3.0 μm, respectively. Similar to the nanometer-scale InP crystals, crystalline defects inside these

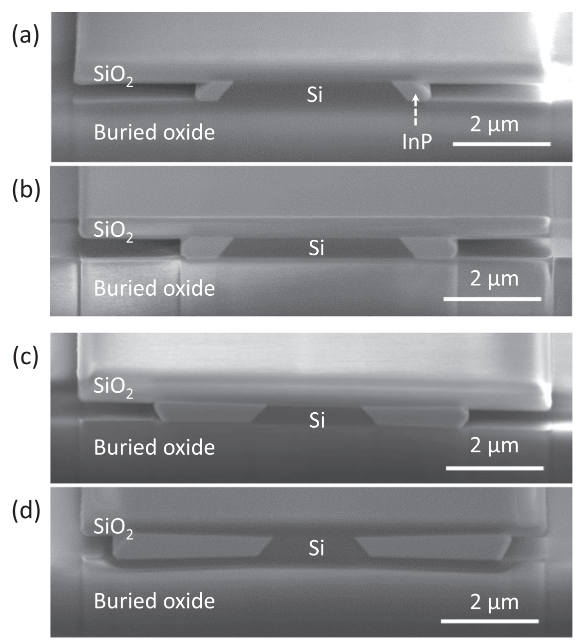

FIG. 2. (a)–(d) Cross-sectional SEM photo of 500 nm, 1.0 μm, 2.0 μm, and 3.0 μm wide InP grown on SOI, respectively.

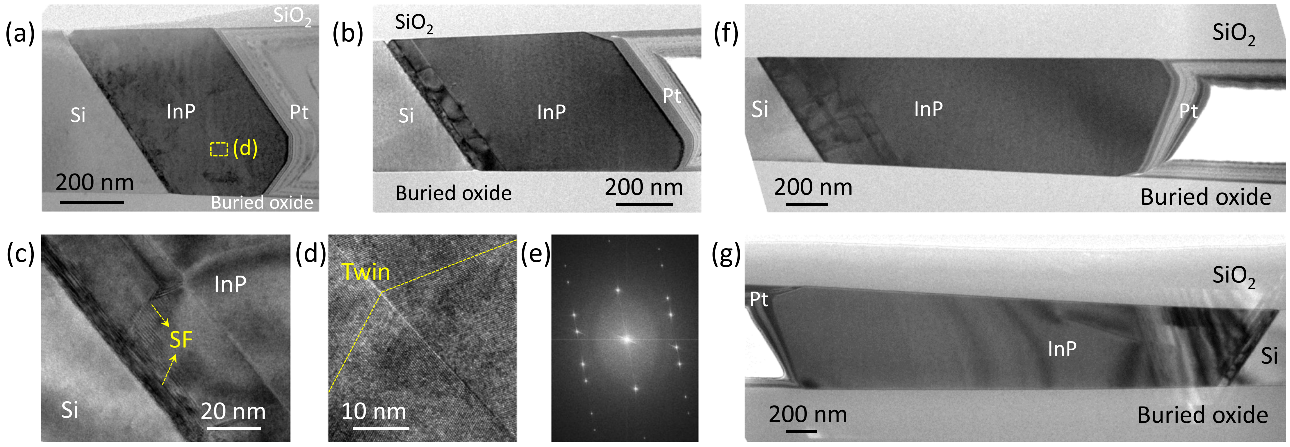

FIG. 3. (a), (b), (f), and (g) Cross-sectional TEM photo of 500 nm, 1.0 μm, 2.0 μm, and 3.0 μm wide InP grown on SOI, respectively. (c) Zoomed-in TEM photo of the III–V/Si interface. (d) High-resolution TEM photo of one {111}-oriented twin. (e) Diffraction pattern of the twin with two sets of InP lattices.

micrometer-scale InP are located near the III–V/Si interface and a majority portion of the InP crystal is dislocation-free. As indicated by the TEM photos, the growth front of the InP changes as the crystal evolves laterally along the trench direction. Initially, the growth front of the InP is purely {111}-oriented, the same as the etched Si surface. As epitaxy continues, the growth front gradually evolves into a multi-faceted surface and varies along the lateral trenches. We attribute this variation to the different growth conditions experienced by the growth front as the diffusion of indium and phosphorus adatoms differs inside the deep lateral trench. As expected, a pure {111}-oriented growth front often introduces twinning during growth. Figure 3(d) displays a high-resolution TEM image of one twin located close to the III–V/Si interface [see Fig. 3(a)]. We detected two sets of InP lattices mirrored by the {111}-oriented twin, as evidenced by a yellow dotted line in Fig. 3(d) and the diffraction pattern in Fig. 3(e). As twins often appear when the growth front manifests a single {111}-oriented facet,[24] formation of twins can be avoided via creation of non-{111}-oriented growth fronts through fine-tuning the growth parameters.

We then characterized the micrometer-scale InP grown on SOI using high resolution x-ray diffraction (XRD) measurements. Figure 4(a) plots the measured ω-rocking curves of the 3.0 μm wide InP grown on SOI. The schematics shown in Fig. 4(b) illustrate the measurement setup and denote the orientation of the x-ray beam relative to the trench direction of the sample. The line-shaped x-ray spot exhibits a length of 12 mm and a width of around 1.8 mm. When the trench direction was positioned parallel to the x-ray beam, we observed two diffraction peaks from the epitaxial InP, corresponding to the symmetrical InP crystals grown from the central Si pedestal [see Fig. 2(d)]. As the trench direction gradually rotates perpendicular to the x-ray beam, the two diffraction peaks progressively shift and eventually merge into a single peak. This position shift of the diffraction peak as the sample rotates suggests a tilt of the InP lattice with respect

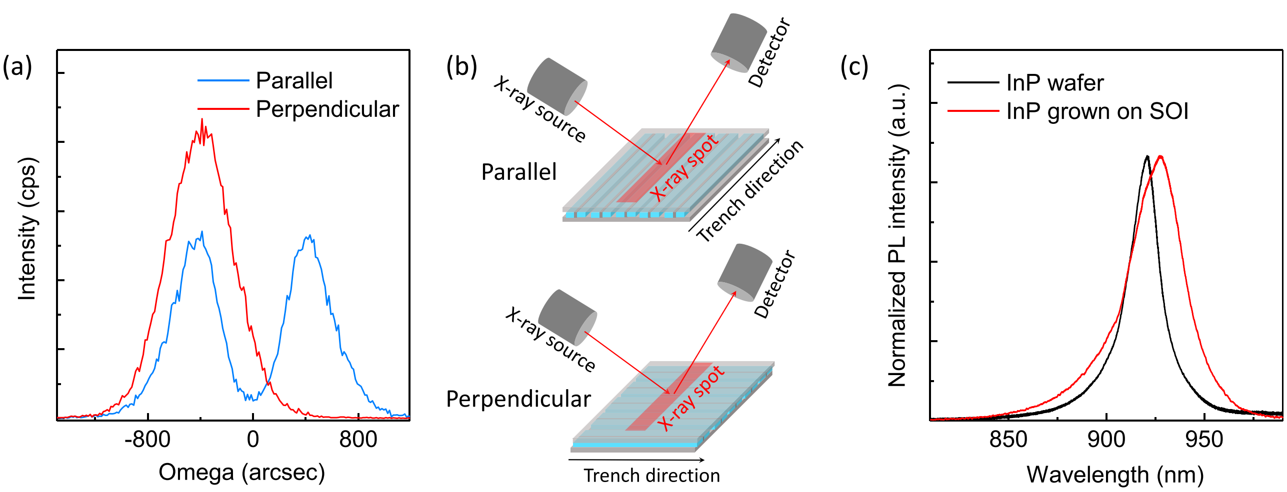

FIG. 4. (a) XRD measurements of the 3.0 μm wide InP grown on SOI with the trench direction parallel and perpendicular to the trench direction. (b) Schematics illustrating the orientation of the x-ray beam relative to the trench direction of the sample. (c) Room temperature photoluminescence spectra of InP wafers and the 3.0 μm InP selectively grown on SOI.

to the Si device layer and a different tilt direction of the two symmetrical InP crystals. The lattice tilt of III–V layers grown on Si substrates has long been noticed and is attributed to the plastic strain relaxation.[25] The full-width-half-maximum of the InP diffraction peak is around 389 arc sec, which is comparable to that of micrometer-thick InP grown on planar Si wafers.[26] Note that the diffraction peak is broadened by the defective InP close to the III–V/Si interface, and the defect density significantly reduces as the InP grows away from the hetero-interface benefiting from the defect necking effect of the oxide masks. The weak diffraction signal of the InP on SOI resulted from the limited overall material volume. We also probed the optical properties of the 3.0 μm wide InP grown on SOI and compared it with InP wafers with perfect lattices. Figure 4(c) displays the measured room temperature photoluminescence spectra. The InP wafer exhibits a peak wavelength of 920 nm and a FWHM of 20 nm, while the epitaxial InP on SOI features a peak wavelength of 927 nm and a FWHM of 31 nm. The FWHM of micrometer-scale InP grown on SOI is significantly reduced compared with that of nanometer-scale InP on SOI (around 57 nm) grown at similar temperatures.[21] We ascribe the slight peak shift of the epitaxial InP with respect to the InP wafer to the incorporated impurities during material deposition and the residual strain induced by lattice mismatch. Similar to the XRD measurements, the photoluminescence emission of the epitaxial InP is also slightly compromised by the defective InP close to the III–V/Si interface as the photo-generated carriers can diffuse to the defective region and recombine there.

The epitaxial InP on SOI can serve as buffer layers for the growth of InGaAs quantum structures emitting at telecom wavelengths. We incorporated five InGaAs quantum wells inside the lateral InP crystals, as shown by the cross-sectional TEM image in Fig. 5(a). The quantum wells are embedded at positions away from the III–V/Si interface to obviate the influences of crystalline defects. As a result of the multi-faceted growth front, the InGaAs quantum wells consist of three different components: the upper {111}-oriented quantum well, the middle quantum well enclosed by higher order transitional facets, and the bottom {111}-oriented quantum well, as schematically delineated in Fig. 5(b). The thicknesses of the quantum wells vary, with a thick bending (~30 nm) separating the upper part (~7 nm) and the bottom part (~2 nm). The thick "elbow" of the quantum wells results from the growth preference of InGaAs at the curved InP corner.[12] Despite the thickness variation, the InGaAs/InP quantum wells feature atomic sharp interfaces, as illustrated by the zoomed-in TEM photo in Fig. 5(c). Optical properties of the as-grown quantum wells were investigated by micro-photoluminescence measurements, and the result is shown in Fig. 5(d). The broad spontaneous emission spectrum is attributed to the variation of the quantum well thickness and the composition fluctuation of the central quantum wells. Note that the growth front of the laterally evolved InP can be fine-tuned into different geometries,[27] suggesting the flexibility in forming quantum structures with different architectures. One example includes the selection of the lasing modes through growing quantum wells with different orientations.[28] We also observed a few equally spaced resonance peaks from the photoluminescence spectra. These peaks are not directly correlated with the quantum wells with different thicknesses. Instead, they stem from light oscillation inside the cavity depicted in the inset of Fig. 5(d). The lateral cavity is composed of two symmetrical InP crystals and one central Si pedestal. Sandwiched between low index SiO_2 layers,

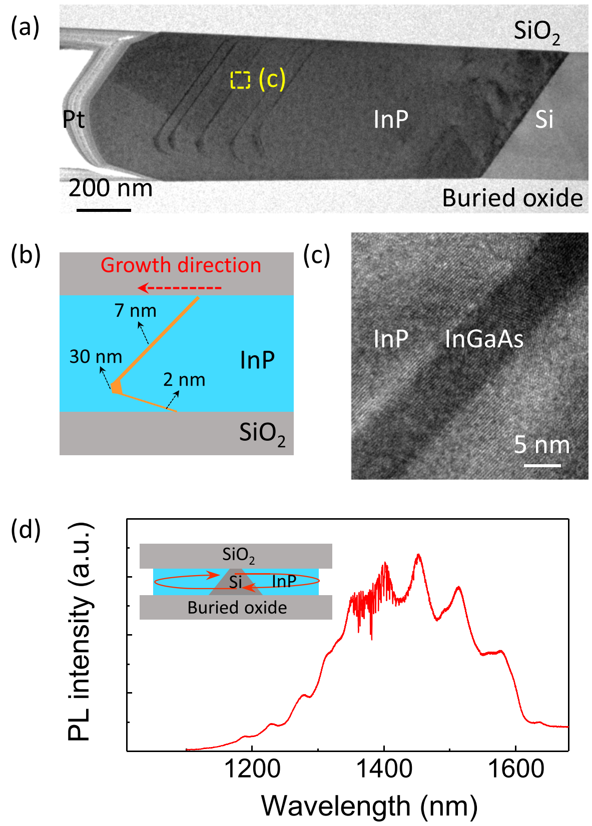

FIG. 5. (a) Cross-sectional TEM image of InGaAs/InP quantum wells laterally grown on SOI. (b) Schematic showing the three quantum wells with different thicknesses. The red dotted arrow denotes the growth direction. (c) Zoomed-in TEM photo of the 7 nm thick top InGaAs quantum well. (d) Room temperature photoluminescence emission spectrum of the InGaAs quantum wells. The sharp line dips result from the water vapor absorption. The inset is a schematic illustrating light oscillation inside the cavity composed of two symmetrical InP crystals and the central Si pedestal.

light generated during the photoluminescence measurement was confined inside the lateral cavity and then amplified into resonance peaks as it traveled in multiple round-trips. The free-spectral-range (~60 nm at 1500 nm) of the photoluminescence peaks also agrees with the length of the lateral cavity (~5.0 μm).

We investigated the potential of employing the micrometer-scale InP for electrically driven lasers on SOI using numerical simulation and focused on the study of optical loss induced by metal contacts. Figure 6(a) sketches the layout of the designed laser grown by the lateral ART method, and Fig. 6(b) details the cross-sectional schematic of the simulated structure. The laterally evolved InP is doped into p–i–n junctions with the active region etched into a ridge structure and the metal contacts patterned at both ends. Doping can also be performed after the material deposition using ion implantation and thermal diffusion. As the InP resides atop the buried oxide layer, light can be tightly confined within the epitaxial InP. The propagation loss thereby mainly results from light absorption by the metal contacts. The length of the epitaxial InP is set as 3.0 μm and the height is set as 500 nm, similar to

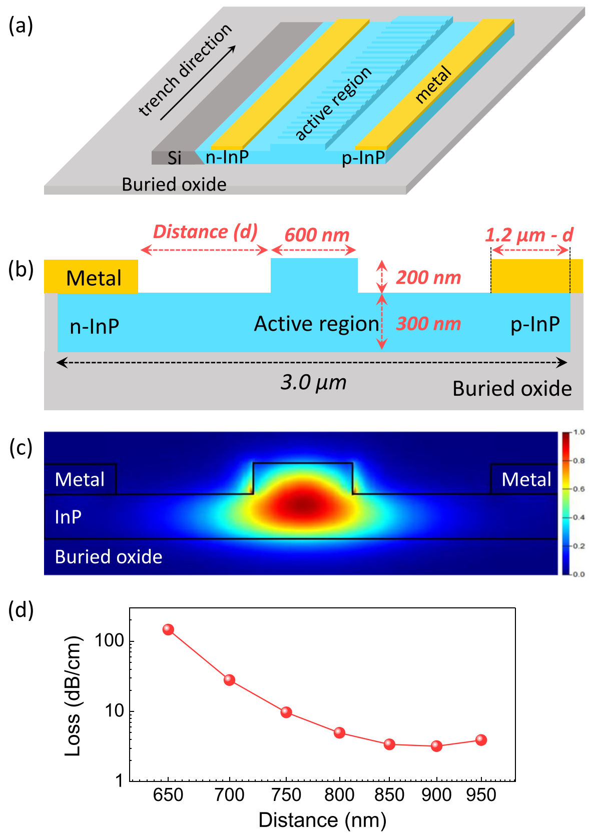

FIG. 6. (a) Schematic illustrating the layout of the designed laser grown on SOI by the lateral ART method. (b) Cross-sectional schematic of the simulated laser structure. (c) Calculated profile of the fundamental TE mode supported inside the InP ridge waveguide. The distance between the metal contact and ridge is 800 nm. (d) Calculated propagation loss induced by metal contacts of the fundamental TE mode inside the InP ridge waveguide as the length between the metal pads and the ridge structure increases.

the micrometer-scale InP grown on SOI presented earlier. The width of the ridge is designed as 600 nm and the depth is devised as 200 nm. We evaluated the metal-induced optical loss through varying the distance (denoted by d) between the metal contacts and the central ridge structure. The contact area between the metals and the epitaxial InP changes accordingly and is described by the equation: $1.2\,\mu m - d$ [see the schematic in Fig. 6(b)]. As shown by the calculated values plotted in Fig. 6(d), the metal-induced propagation loss of the fundamental TE mode at $1.5\,\mu m$ decreases exponentially from over 100 dB/cm to 3.2 dB/cm as d progressively increases from 650 nm to 850 nm. Figure 6(c) displays the profile of the fundamental TE mode with d set as 800 nm. The mode is tightly confined within the central ridge structure and manifests minimal overlap with the metal contacts. The drastic reduction of the propagation loss highlights the significance of growing large-dimension InP crystals on SOI.

In conclusion, we demonstrated the direct hetero-epitaxy of micrometer-scale InP on industry-standard (001) SOI wafers for future fully integrated Si-photonics. Through leveraging our lateral ART growth method and creating ultra-wide lateral oxide trenches, we obtained in-plane InP crystals with dimensions ranging from the nanometer-scale up to a few micrometers. Crystalline defects are confined at the III–V/Si interface, rendering InP away from the interface completely dislocation-free. The theoretical calculation suggests an ultra-low metal induced propagation loss of 3.2 dB/cm when patterning the micrometer-scale InP into ridge waveguides and introducing metal contacts at both ends. These large-dimension InP crystals can be employed to fabricate lasers, modulators, and photo-detectors seamlessly integrated onto current Si-photonics platforms.

AUTHORS' CONTRIBUTIONS

Y.H. and Z.Y. contributed equally to this work.

This work was supported by the Research Grants Council, University Grants Committee (Nos. 16212115 and 16245216), and Innovation and Technology Fund (No. ITS/273/16FP). The authors thank the MCPF and NFF of HKUST for technical support. Helpful discussions with C. W. Tang are also acknowledged.

DATA AVAILABILITY

The data that support the findings of this study are available from the corresponding author upon reasonable request.

REFERENCES

[1]Z. Wang, A. Abbasi, U. Dave, A. De Groote, S. Kumari, B. Kunert, C. Merckling, M. Pantouvaki, Y. Shi, B. Tian, K. Van Gasse, J. Verbist, R. Wang, W. Xie, J. Zhang, Y. Zhu, J. Bauwelinck, X. Yin, Z. Hens, J. Van Campenhout, B. Kuyken, R. Baets, G. Morthier, D. Van Thourhout, and G. Roelkens, Laser Photonics Rev. **11**, 1700063 (2017).
[2]A. Y. Liu and J. Bowers, "Photonic integration with epitaxial III-V on silicon," IEEE J. Sel. Top. Quantum Electron. **24**, 6000412 (2018).
[3]Q. Li and K. M. Lau, Prog. Cryst. Growth Charact. Mater. **63**(4), 105–120 (2017).
[4]B. Kunert, Y. Mols, M. Baryshniskova, N. Waldron, A. Schulze, and R. Langer, Semicond. Sci. Technol. **33**(9), 093002 (2018).
[5]D. Jung, R. Herrick, J. Norman, K. Turnlund, C. Jan, K. Feng, A. C. Gossard, and J. E. Bowers, Appl. Phys. Lett. **112**, 153507 (2018).
[6]A. Y. Liu, S. Srinivasan, J. Norman, A. C. Gossard, and J. E. Bowers, Photonics Res. **3**(5), B1–B9 (2015).
[7]B. Shi, Y. Han, Q. Li, and K. M. Lau, IEEE J. Sel. Top. Quantum Electron. **25**, 1 (2019).
[8]T. Zhou, M. Tang, G. Xiang, B. Xiang, S. Hark, M. Martin, T. Baron, S. Pan, J. S. Park, Z. Liu, S. Chen, Z. Zhang, and H. Liu, Nat. Commun. **11**(1), 977 (2020).
[9]S. Wirths, B. F. Mayer, H. Schmid, M. Sousa, J. Gooth, H. Riel, and K. E. Moselund, ACS Nano **12**, 2169–2175 (2018).
[10]Y. Han, Q. Li, S. P. Chang, W. D. Hsu, and K. M. Lau, Appl. Phys. Lett. **108**, 242105 (2016).
[11]B. Kunert, W. Guo, Y. Mols, B. Tian, Z. Wang, Y. Shi, D. Van Thourhout, M. Pantouvaki, J. Van Campenhout, R. Langer, and K. Barla, Appl. Phys. Lett. **109**, 091101 (2016).
[12]Y. Han, Q. Li, K. W. Ng, S. Zhu, and K. M. Lau, Nanotechnology **29**, 225601 (2018).
[13]Z. C. Wang, B. Tian, M. Pantouvaki, W. M. Guo, P. Absil, J. V. Campenhout, C. Merckling, and D. V. Thourhout, Nat. Photonics **9**(12), 837–842 (2015).
[14]Y. Han, Z. Yan, W. K. Ng, Y. Xue, K. S. Wong, and K. M. Lau, Optica **7**(2), 148–153 (2020).
[15]Y. Shi, Z. Wang, J. Van Campenhout, M. Pantouvaki, W. Guo, B. Kunert, and D. Van Thourhout, Optica **4**, 1468 (2017).
[16]Y. Han, K. W. Ng, Y. Xue, Q. Li, K. S. Wong, and K. M. Lau, Opt. Lett. **44**(4), 767–770 (2019).
[17]B. F. Mayer, S. Wirths, S. Mauthe, P. Staudinger, M. Sousa, J. Winiger, H. Schmid, and K. E. Moselund, IEEE Photonics Technol. Lett. **31**(13), 1021–1024 (2019).

[18]Y. Han, W. K. Ng, C. Ma, Q. Li, S. Zhu, C. C. S. Chan, K. W. Ng, S. Lennon, R. A. Taylor, K. S. Wong, and K. M. Lau, Optica **5**, 918 (2018).
[19]Y. Han, K. W. Ng, Y. Xue, K. W. Ng, K. S. Wong, and K. M. Lau, Appl. Phys. Lett. **116**, 172102 (2020).
[20]G. Crosnier, D. Sanchez, S. Bouchoule, P. Monnier, G. Beaudoin, I. Sagnes, R. Raj, and F. Raineri, Nat. Photonics **11**(5), 297 (2017).
[21]Y. Han, Y. Xue, and K. M. Lau, Appl. Phys. Lett. **114**, 192105 (2019).
[22]M. Paladugu, C. Merckling, R. Loo, O. Richard, H. Bender, J. Dekoster, W. Vandervorst, M. Caymax, and M. Heyns, Cryst. Growth Des. **12**, 4696–4702 (2012).
[23]O. Parillaud, E. Gil-Lafon, B. Gerard, P. Etienne, and D. Pribat, Appl. Phys. Lett. **68**(19), 2654–2656 (1996).
[24]M. Knoedler, N. Bologna, H. Schmid, M. Borg, K. E. Moselund, S. Wirths, M. D. Rossell, and H. Riel, Cryst. Growth Des. **17**(12), 6297–6302 (2017).
[25]M. Grundmann, A. Krost, and D. Bimberg, Surf. Sci. **267**(1–3), 47–49 (1992).
[26]B. Shi, Q. Li, and K. M. Lau, J. Appl. Phys. **123**(19), 193104 (2018).
[27]S. T. Šuran Brunelli, A. Goswami, B. Markman, H. Y. Tseng, M. Rodwell, C. Palmstrøm, and J. Klamkin, Cryst. Growth Des. **19**(12), 7030–7035 (2019).pp.
[28]L. A. Coldren and S. W. Corzine, *Diode Lasers and Photonic Integrated Circuits* (Wiley, 2012).